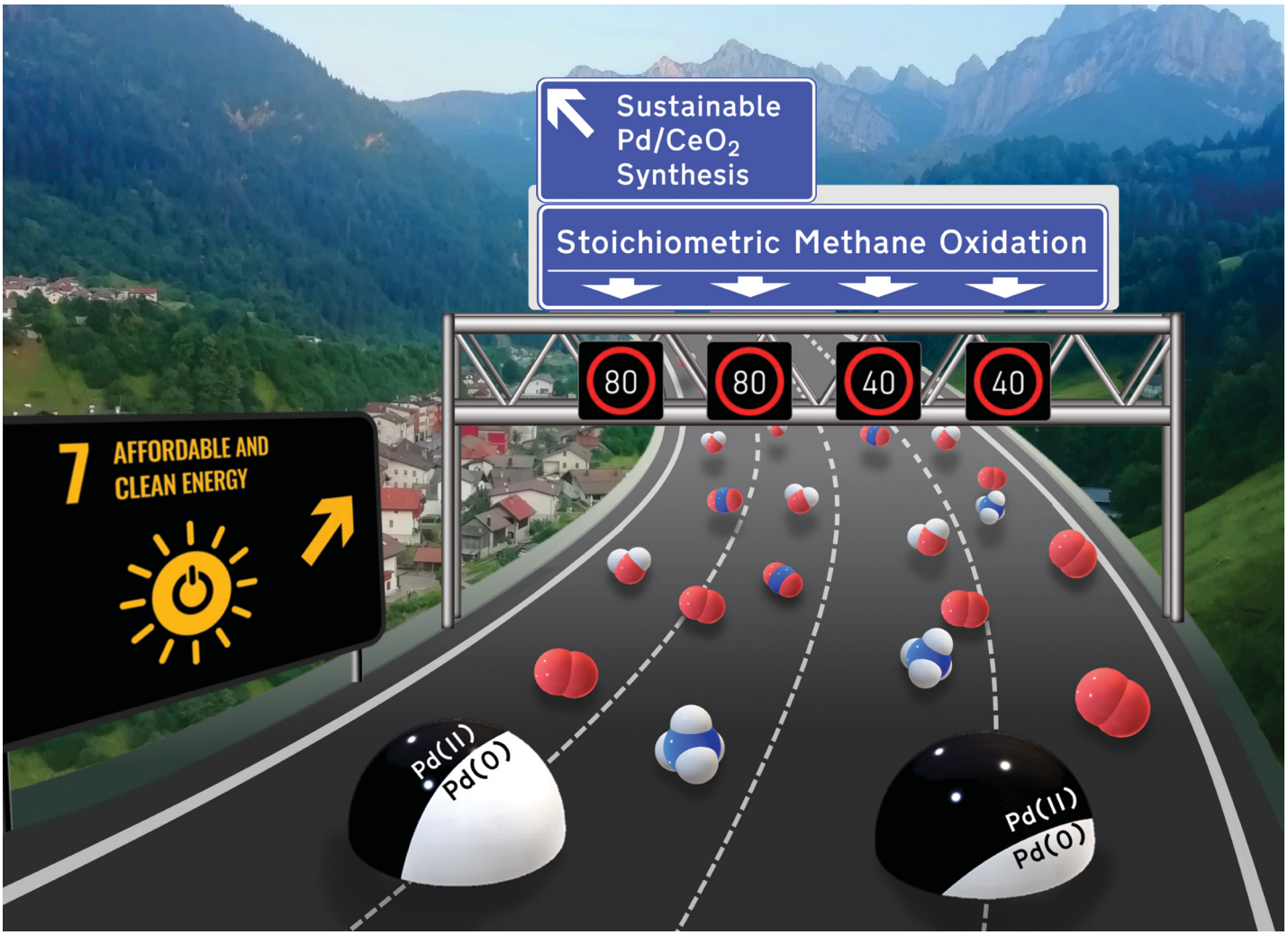

Showcasing research on palladium-ceria heterogeneous catalysts for environmental applications from Professor Alessandro Trovarelli's laboratory, Catalysis for Energy and Environment Group, Polytechnic Department, University of Udine, Italy.

In situ investigation of the mechanochemically promoted Pd–Ce interaction under stoichiometric methane oxidation conditions

Pd entities supported on ceria by a dry milling method maintain a peculiar configuration with a balanced ratio between reduced Pd^0 and oxidized Pd^{2+} species, leading to high turnover in CH_4 oxidation and improved resistance to steam deactivation even under low oxygen availability. The results were obtained combining innovative materials preparation and testing at the University of Udine with *in situ* analysis at the Universitat Politècnica de Catalunya and the Chemistry Division of Brookhaven National Laboratory. Image illustrated by Dr Maila Danielis.

As featured in:

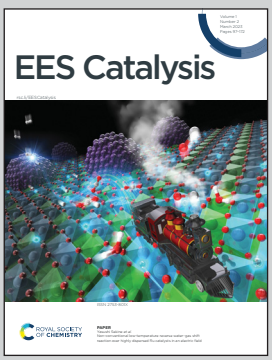

See Alessandro Trovarelli *et al.*, *EES. Catal.*, 2023, **1**, 144.

ROYAL SOCIETY OF CHEMISTRY

rsc.li/EESCatalysis

Registered charity number: 207890

EES Catalysis

PAPER

View Article Online
View Journal | View Issue

Cite this: *EES Catal.*, 2023, 1, 144

In situ investigation of the mechanochemically promoted Pd–Ce interaction under stoichiometric methane oxidation conditions†

Maila Danielis,[a] Núria J. Divins,[bc] Jordi Llorca,[bc] Lluís Soler,[bc] Xènia Garcia,[bc] Isabel Serrano,[b] Luis E. Betancourt,[d] Wenqian Xu,[e] José A. Rodríguez,[d] Sanjaya D. Senanayake,[d] Sara Colussi[a] and Alessandro Trovarelli*[a]

Received 9th October 2022,
Accepted 7th December 2022

DOI: 10.1039/d2ey00067a

rsc.li/eescatalysis

The optimization of the supported Pd phase for CH_4 activation on Pd/CeO_2 catalysts has been a matter of great interest in the recent literature, aiming at the design of efficient methane abatement catalysts for Natural Gas fueled Vehicles (NGVs). Under lean conditions, a mixed Pd^0/PdO combination has been indicated as exhibiting the best performance, while controversial results have been reported under stoichiometric conditions depending on the support oxide, where either Al_2O_3 or zeolite-based supports are usually considered. Here, by means of synchrotron-based *in situ* NAP-XPS and XRD measurements, we follow the evolution of Pd species on Pd/CeO_2 samples prepared by dry mechanochemical synthesis (M) under stoichiometric CH_4 oxidation feed, unravelling a stable Pd^0/Pd^{2+} arrangement in a close to 1 : 1 ratio as the most active palladium state for CH_4 activation when excess oxygen is not available, in contrast to what was reported for Pd/alumina materials, where metallic Pd^0 nanoparticles showed the highest activity. The combination of NAP-XPS analysis and activity test results highlights the promotional effect of the Pd–Ce interaction, resulting in enhanced oxygen transfer and improved activity and stability of the Pd/CeO_2 catalyst prepared by a novel mechanochemical approach even under low O_2 content, large excess of water vapor (10 vol%) and high temperature exposure (>700 °C).

Broader context

The increasing global energy demand coupled with the imperative need to decrease greenhouse gas (GHG) emissions has strongly pushed in recent years towards the research and development of more sustainable energy sources. Amidst the various possible alternatives to liquid fossil fuels, natural gas (NG) has proved to be a feasible transition fuel while hydrogen- and electric-technologies become socially and commercially available. Increasing NG use would also serve as a cleaner alternative to flaring, which is especially common near oil-drilling sources. However, methane itself is a strong greenhouse gas and its utilization should be strictly controlled. For this reason, catalytic materials have to be optimized to ensure full methane conversion at low temperature, whether for abatement applications or for CH_4 transformation into value-added chemicals. Here, we investigate in detail the surface interaction generated by dry milling between cerium oxide and palladium, specifically for enhanced activation of methane under stoichiometric conditions for unburned CH_4 emission control. The insights gained regarding the metal–support interactions and their interplay for promoted CH_4 conversion can be of general interest for the design of tailored methane valorization catalysts, reducing the amount of noble metal and relying on a more sustainable synthesis method such as mechano-chemistry.

[a] *Dipartimento Politecnico, Università di Udine, and INSTM, via del Cotonificio 108, 33100 Udine, Italy. E-mail: alessandro.trovarelli@uniud.it*
[b] *Institute of Energy Technologies and Department of Chemical Engineering, Universitat Politècnica de Catalunya, EEBE, Eduard Maristany 10-14, 08019 Barcelona, Spain*
[c] *Barcelona Research Center in Multiscale Science and Engineering, Universitat Politècnica de Catalunya, EEBE, Eduard Maristany 10-14, 08019 Barcelona, Spain*
[d] *Chemistry Division, Brookhaven National Laboratory, Upton, NY 11973, USA*
[e] *X-Ray Science Division, Advanced Photon Source, Argonne National Laboratory, Lemont, IL 60439, USA*

† Electronic supplementary information (ESI) available. See DOI: https://doi.org/10.1039/d2ey00067a

Introduction

Considering the significant contribution of the mobility sector to the global emission of greenhouse gases (GHGs), the need for sustainable alternative fuels and efficient after-treatment systems is of utmost importance in order to reach the decarbonization goals set forth by the EU and UN for the next few decades[1,2] and ensure improved air quality.[3] Among others, the substitution of traditional fossil fuels by natural gas appears to be a promising, ready-to-go option in the transition towards

fully electric or H_2-fueled fleets.[4–6] The low C : H ratio of methane, the main component of natural gas, ensures lower production of CO_2, NO_x, and soot particulates in the engine compared to other fossil fuels,[5,7,8] and its facile substitution by biomethane coupled with the well-developed natural gas distribution grids has already pushed towards a significant diffusion of natural gas fueled vehicles (NGVs) in recent decades.[9]

However, unburned CH_4 is a strong greenhouse gas and its leakage needs to be carefully controlled.[6,10,11] In the engine, the combustion technology of choice (stoichiometric *vs.* lean) depends on the desired power and torque requirements of the vehicle,[12,13] and subsequently affects the catalytic after-treatment conditions.[14,15] Platinum Group Metal (PGM)-based catalysts have been implemented to burn residual methane in the exhaust gases of NGVs to ensure abatement within imposed legislation limits,[11] as either oxidative catalysts (OCs) for lean burn engine technologies or as three-way catalysts (TWCs) in stoichiometric engines.[16,17] Stoichiometric methane oxidation represents a different system compared to excess O_2 conditions,[13,15] presenting several challenges in terms of oxidation states and stability of PdO species and the possible occurrence of other predominant reactions (partial methane oxidation, steam reforming).[18] The stoichiometric point, indeed, often represents the most difficult lambda range for three-way catalyst development.[11]

In the latter context, Pd-based catalysts are currently reported as the most active for CH_4 abatement;[17,19–21] however, they are also characterized by low resistance to deactivation in the presence of steam under an O_2-poor atmosphere and are susceptible to thermal aging.[14,22–24] Thus, most recent efforts are aimed at improving the performances of Pd catalysts in these aspects. One widely employed solution is the addition of Pt to Pd-based catalysts,[25–28] yet the optimization of the Pd phase is also highly desirable to improve catalytic activity and stability without increasing the noble metal loading and overall cost of the after-treatment system.[29–31] In this regard, many recent studies have focused on the effect of optimal PdO particle size and of the oxidation state transitions in Pd/Al_2O_3-based samples during lean/rich switches and under isothermal conditions (<773 K).[32–36] On these samples, CeO_2 addition was observed to stabilize the oxidized PdO species thanks to its oxygen storage capacity,[36–39] while Pd^0 species led to higher activity on pure Pd/Al_2O_3 materials.[33,34] Similar findings were reported for zeolite-supported Pd catalysts, where the stabilization of Pd^{2+} ions in the SSZ-13 structure resulted in decreased catalytic performance.[40] Nevertheless, to the best of our knowledge a comprehensive study on Pd/CeO_2 catalysts under stoichiometric methane oxidation after-treatment conditions has not yet been reported, including the effects of the co-presence of H_2O and high temperature exposure, which are necessary to evaluate the catalyst's resistance to thermal aging.[41]

We have recently reported the development of a Pd/CeO_2 catalytic system obtained by solvent-free mechanochemical synthesis which yields a combination of undercoordinated Pd^0/Pd^{2+} sites in close contact with the surface ceria lattice, thus leading to enhanced methane conversion performance in lean conditions[42,43] and under industrial bench test conditions,[44] which range from lean oxidation to steam reforming in rich CH_4 feed. Here, we investigate the evolution of the supported Pd species under a stoichiometric feed (1 : 2 CH_4 : O_2), followed by means of *in situ* XRD and NAP-XPS techniques. The effect of the unique Pd–Ce interaction on the catalytic activity of Pd/CeO_2 samples in dry and wet conditions was thoroughly investigated, aiming at filling the gap on the most active Pd species for methane conversion under stoichiometric CH_4 : O_2 pressure.

Experimental

Catalyst synthesis

4 wt% Pd/CeO_2 samples were prepared on commercial ceria (Rhodia), and calcined at 1173 K in static air for 3 hours before noble metal loading (surface area: 25 $m^2\ g^{-1}$). Pd was dispersed on the support by dry mechano-chemical synthesis (M) and incipient wetness impregnation (IW) following established synthesis routes reported elsewhere.[42] Briefly, for the milled sample (4PdAcCeM), 84.4 mg of palladium acetate (Sigma-Aldrich, 99.9%) and 960 mg of CeO_2 were milled for 20 minutes in a 15 mL ZrO_2 milling jar loaded with one ZrO_2 grinding ball (15 mm diameter, *ca.* 10 g weight) using a Pulverisette 23 mini-mill operating at 15 Hz. The reference 4PdCeIW sample was prepared by incipient wetness impregnation, wetting 1 g of CeO_2 powder with an appropriate amount of commercial palladium nitrate solution (Sigma-Aldrich, 99.999%) to reach a final Pd loading of 4 wt%. After complete wetting, the powders were dried at 373 K overnight and subsequently calcined at 1173 K for 3 h in static air. A high metal loading (4 wt%) was chosen to obtain a stronger signal and a higher definition from AP-XPS and XRD techniques, where the surface and catalytic properties can be considered representative also of lower Pd loadings.[42]

Ex situ catalyst characterization

The surface area and pore volume of the prepared samples were investigated by analysis of N_2 adsorption isotherms at 77 K in a Micromeritics Tristar 3000 analyzer using BET and BJH methods, respectively. ICP-MS analysis, performed by Mikroanalytisches Labor Pascher (Remagen, Germany), was used to measure the amount of loaded Pd on the prepared samples. *Ex situ* Raman spectroscopy was used to probe the surface Pd and CeO_2 states before and after the reaction. Raman spectra were collected using an Xplora Plus Micro-Raman system (Horiba, Kyoto, Japan) using a 532 nm laser source. The spectra were acquired at room temperature with a resolution of 1 cm^{-1} and 5 accumulations of 60 s with a 50× LWD objective. Temperature Programmed Oxidation (TPO) analysis was carried out to probe the decomposition-reoxidation behavior of the supported Pd samples. For TPO tests, 150 mg of catalyst powder were placed in a quartz reactor supported on a quartz wool bed. The sample was then exposed to a flowing mixture

(60 mL min^{-1}) containing 2 vol% O_2 in N_2, and the oxygen release and consumption was monitored with an ABB Magnos 106 paramagnetic analyzer during 3 heating/cooling cycles (from RT up to 1273 K, at a heating/cooling ramp of 10 K min^{-1}).

In situ catalyst characterization

Time-resolved XRD measurements were performed at beamline 17 BM (λ = 0.24169 Å) at the Advanced Photon Source (APS) in Argonne, IL, using a Clausen cell flow reactor.[45] A 30 mL min^{-1} flow rate of a gas mixture containing 0.3% CH_4, 0.6% O_2 and balance He was introduced, and then the sample was heated to 773 K at a 10 °C min^{-1} ramping rate; two heating/cooling cycles were performed to reach stable behavior. An in-line residual gas analyzer was used to track the evolution of the gaseous species right after the flow cell. A Si flat detector (PerkinElmer) was used to collect two-dimensional XRD images every 60 s throughout the reaction processes. The XRD data were subsequently processed with GSAS-II software.[46]

Information on the surface electronic state during the reaction was gathered by means of Ambient-Pressure X-ray Photoelectron Spectroscopy (AP-XPS) at the CIRCE beamline of the ALBA Synchrotron Light Source, following the surface chemical composition under *operando* conditions at 2 mbar and different temperatures. Different excitation photon energies were used to obtain XP spectra of Ce 3d, O 1s, Pd 3d, and C 1s (acquiring photoelectrons with photon energy 485 eV (kinetic energy – KE – 150 eV), corresponding approximately to 0.5 nm inelastic mean free path (IMFP), photon energy 682 eV (KE 350 eV, IMFP = 0.9 nm) and photon energy 1032 eV (KE 700 eV, IMFP = 1.4 nm)). Catalyst powders were pressed with a gold mesh with a 0.25 mm nominal aperture (99.9%, GoodFellow) to form a compact disk and to minimize charging effects. The AP-XPS spectra were measured with a commercial PHOIBOS 150 NAP energy analyzer, equipped with four differentially pumped stages. Methane (0.6 mbar) and oxygen (1.4 mbar) were dosed into the analysis chamber by high-precision leak valves. The evolution of products was followed by a quadrupole mass spectrometer Microvision 2 Residual Gas Analyzer (MKS Instruments). Samples were heated using an infrared laser (λ = 808 nm) focused on a stainless-steel plate on top of which the samples were mounted. The temperature was monitored with a K-type thermocouple in contact with the samples. Due to the upper temperature limits of the XPS chamber, samples were pretreated *ex situ* by running a complete methane oxidation test up to 1173 K before analysis. Data processing was performed with the CasaXPS program (Casa Software Ltd, UK). To compensate the charging effects, spectra were calibrated with respect to the U‴ Ce 3d peak at 916.8 eV.[47,48] Atomic fractions were calculated using peak areas normalized on the basis of acquisition parameters after background subtraction. The relative sensitivity factors were calculated taking into account the ionization cross-section of each spectral region,[49] the photon flux corresponding to the photon energy used for each measurement, and the transmission function of the analyzer. Cerium 3d spectra were deconvoluted using six peaks for Ce^{4+} (V, V″, V‴, U, U″ and U‴), which correspond to three pairs of spin–orbit doublets, and four peaks for Ce^{3+} (V_0, V′, U_0 and U′), corresponding to two doublets, based on the peak positions reported by Mullins *et al.*,[47] where U and V refer to the $3d_{3/2}$ and $3d_{5/2}$ spin–orbit components, respectively.

Catalytic activity tests

Methane oxidation tests were carried out on 30 mg of catalyst powder, loaded on a quartz wool bed in a quartz reactor (ID 6 mm) and placed inside of a tubular furnace. For standard Temperature Programmed Combustion (TPC) tests, the sample was exposed to 90 mL min^{-1} of a high precision 0.5%CH_4/1%O_2/He gas mixture (SIAD) and heated up to 1173 K at a 10 K min^{-1} heating rate; two heating/cooling cycles were performed, and the second cycle is reported as representative of catalytic activity unless otherwise stated. To evaluate the effect of excess steam, TPC experiments in ''wet'' conditions were performed by adding 10 vol% water vapor to the stoichiometric gas feed, introducing 0.007 mL min^{-1} of liquid water through heated lines using a high-performance liquid chromatography (HPLC) pump. Time-on-stream (TOS) stability tests, in both dry and wet conditions, were performed holding the sample at 723 K for 24 hours; one oxidation cycle up to 1173 K in dry conditions was always performed as pretreatment.

Reaction rates were calculated using methane conversion values below 5% to ensure the kinetic regime; conversion values were measured during the 2nd light off heating ramp of TPC experiments at 563 K and 613 K for dry and wet gas feed, respectively.

Results and discussion

The textural and morphological properties of the 4 wt%Pd/CeO_2 samples obtained by milling (4PdAcCeM) and by the incipient wetness impregnation method (4PdCeIW) were studied by means of BET and XRD analysis, and the actual Pd loading was measured by ICP-MS analysis. The measured surface area and Pd loading are summarized in Table 1.

Temperature programmed oxidation (TPO) experiments were performed to evaluate the redox behavior of the supported Pd species and to assess the amount of loaded palladium undergoing the characteristic PdO–Pd–PdO decomposition–reoxidation hysteresis on both samples. TPO tests were carried out under 1 vol% O_2 and 2 vol% O_2 in N_2, representing the experimental conditions for stoichiometric and lean CH_4 oxidation, respectively, with respect to 0.5 vol% CH_4 in the feed.

Table 1 Summary of the samples considered in this study; nominal Pd loading 4 wt%

Sample	Calcination temperature (K)	BET S.A. (m^2 g^{-1})	Pore volume (cm^3 g^{-1})	Measured Pd loading (wt%)
4PdCeIW	1173	16	0.09	3.94
4PdAcCeM	1173	22	0.17	3.92

Qualitative analysis of the high temperature decomposition profiles, reported in Fig. S1 (ESI†), shows that the lower availability of O_2 has a negligible effect on the palladium species stabilized on the IW and M samples, with the latter maintaining the high temperature O_2 release contribution corresponding to PdO_x species in strong interaction with the ceria surface.[50] Only a slight shift to lower temperature is observed, as expected by the decrease in O_2 partial pressure.[50] In addition, quantitative analysis of the recorded oxygen uptake and release profiles, reported in Table S1 (ESI†), confirms that palladium undergoes the typical PdO ↔ Pd cycle on both samples in the same amount observed under excess oxygen conditions (2 vol%).

To investigate in detail the bulk and surface structure of the Pd species and their evolution under the reaction conditions, the structural characteristics of the investigated samples were followed by *in situ* XRD under dry stoichiometric methane oxidation gas feed (0.3% CH_4, 0.6% O_2, He to balance) up to a temperature of 773 K. Full time-resolved patterns (Fig. S2, ESI†) show that, even under low O_2 partial pressure, the CeO_2 lattice structure remains unaltered during the reaction and the palladium species are well dispersed. No additional strains in the CeO_2 lattice due to Pd incorporation could be detected, suggesting that no diffusion of oxidic Pd species occurs within the ceria lattice. The time-resolved patterns focused on the PdO–Pd 2θ range (5.2–6.8°) are reported in Fig. 1 to highlight the evolution of the supported Pd species. *In situ* XRD measurements highlight PdO nanoparticles as the predominant species on both samples, with a minor appearance of metallic Pd throughout the reaction. On the IW sample the higher intensity of the reflections corresponding to the (101) and (110) planes of palladium oxide, at 2θ = 5.21° and 6.42°, respectively, indicate larger PdO particles,[42] as observed under lean oxidation conditions[42] and corroborated by *ex situ* Raman spectra collected on the samples, reported in Fig. S3 (ESI†). Accurate Scherrer or Rietveld calculation of the average PdO particle size is hindered by the vicinity of the CeO_2 (111) peak, and hence only a semi-quantitative estimate can be inferred from the XRD profiles. Semi-quantitative Rietveld analysis, performed on the secondary (110) PdO peak at 2θ = 6.42°, results in an estimated particle size of *ca.* 20 nm on 4PdCeIW compared to *ca.* 15 nm on 4PdAcCeM. The large particle size might be due to the elevated temperature of the pretreatment (1173 K). Nevertheless, apart from the slight difference in the calculated PdO particle size, the XRD profiles show negligible differences between the bulk structures of the milled and IW samples.

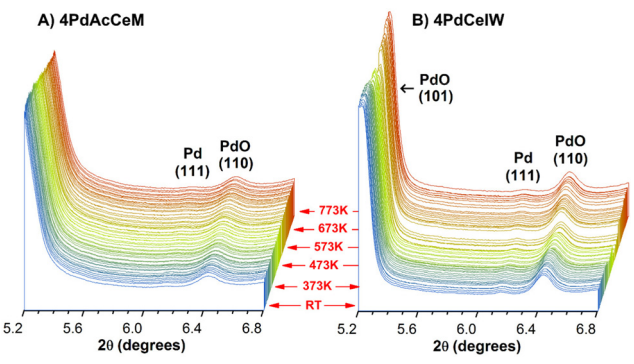

Fig. 1 *In situ* XRD diffraction patterns collected under stoichiometric methane oxidation conditions (0.3% CH_4, 0.6% O_2 in He) on (A) 4PdAcCeM and (B) 4PdCeIW; samples were heated from RT to 773 K at a 10 K min^{-1} heating rate, and scans were collected every 60s.

Consequently, to better understand the reaction mechanisms and the evolution of the catalyst surface states, the oxidation state of palladium and ceria during stoichiometric methane combustion at 673–873 K was followed by Near Ambient Pressure X-ray Photoelectron Spectroscopy (NAP-XPS) experiments. For consistency, both samples were pretreated at 1173 K under the reaction conditions before analysis. As shown in Fig. 2, there are important differences between the surfaces of samples 4PdCeIW and 4PdAcCeM (Fig. 2(A–C) and (D–F), respectively). On the IW sample, only Pd^{2+} and Pd^0 species are detected with no appearance of Pd^{4+}, contrary to what was observed under lean conditions,[42] with the amount of metallic Pd slightly increasing from 14% to 19% with increasing temperature (Fig. 2A). In parallel, a negligible growth of Ce^{3+} is observed (Fig. 2B and Table S2, ESI†). In Fig. 2C, scans in the O 1s range highlight the presence of reaction products (CO_2 and H_2O); however, the surface of the catalyst remains predominantly covered by OH^- species accumulated during the reaction. The milled sample presents a larger amount of Pd in the metallic state, with a remarkable increase in temperature from 22% to 40% (Fig. 2D) and a slightly more significant degree of Ce^{3+} formation (Fig. 2E), suggesting a higher rate of oxygen being removed to react with the CH_4 in the gas feed. Nonetheless, Ce^{4+} is maintained as the predominant species on the 4PdAcCeM sample.

In contrast with what was observed on the IW sample, the M catalyst surface is devoid of hydroxyl groups, and only CO_2 and H_2O products are detected (Fig. 2F). In addition, from the quantitative analysis of the O 1s spectra, reported in Table S2 (ESI†), on the M sample *ca.* 90% of the surface oxygen is found as lattice O–Ce, suggesting that a much higher amount of mobile lattice oxygen is available during reaction to be exchanged to the partially oxidized PdO_x particles. On the other hand, on the IW sample the contribution of the OH^- band accounts for more than 65% of the surface oxygen species. Likely, the surface of the IW sample is more prone to OH formation and stabilization, hence resulting in the blockage of active undercoordinated Pd sites and in slower CH_4 conversion.[51]

Since the surface *vs.* bulk structures of supported PdO particles have been reported as playing a key role in the observed methane dissociation energy,[52,53] NAP-XPS spectra at 873 K were also acquired with different photon energies, *i.e.*, varying the penetration depth, to further investigate the surface, subsurface, and core oxidation states of the supported palladium particles on 4PdCeIW and 4PdAcCeM. Their comparison is reported in Fig. 3, with the corresponding XPS spectra and quantitative analysis reported in full in the ESI†

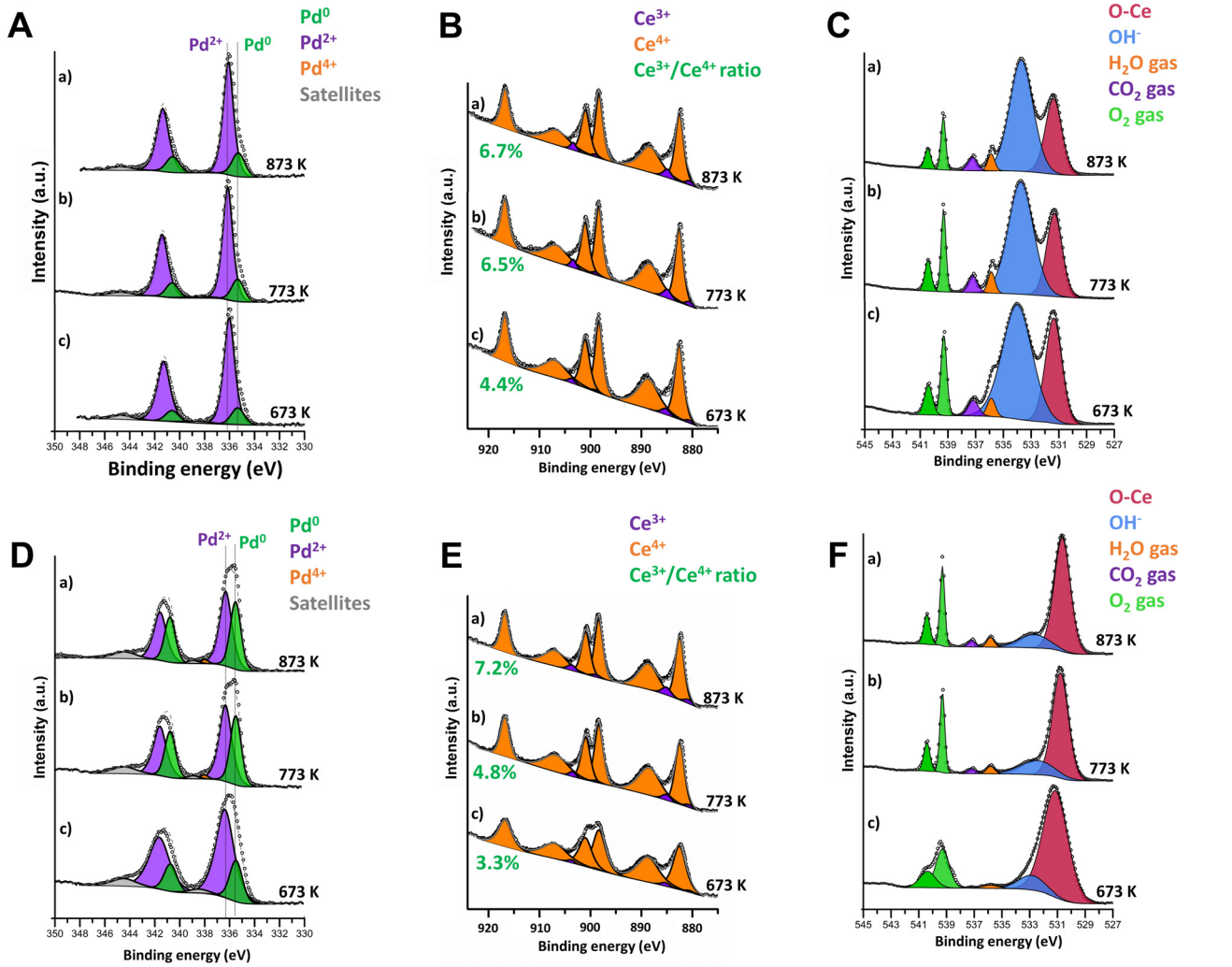

Fig. 2 NAP-XPS spectra collected on 4PdCeIW (A–C) and 4PdAcCeM (D–F) in the Pd 3d (A and D), Ce 3d (B and E) and O 1s (C and F) regions under 0.6 mbar CH_4 and 1.4 mbar O_2 at increasing temperatures: (c) 673 K, (b) 773 K, (a) 873 K.

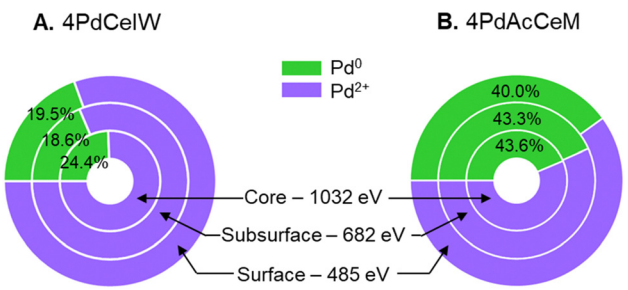

Fig. 3 Comparison of the measured Pd^0/Pd^{2+} amount at different penetration depths on (A) 4PdCeIW and (B) 4PdAcCeM under 0.6 mbar CH_4 and 1.4 mbar O_2 at 873 K.

(Fig. S5 and Table S2). Remarkably, and differently than other supported Pd systems reported in the literature,[32,54] on both samples, the distribution of metallic Pd appears almost uniform throughout the supported PdO_x particles, with a slightly larger amount of oxidized Pd^{2+} on the outermost layers compared to the inner core. The analysis thus confirms that on the milled sample, palladium nanoparticles present a higher contribution of metallic Pd with respect to the impregnated one, irrespective of the probing depth.

The methane oxidation performance of the prepared samples was evaluated in the absence and in the presence of excess water vapor (10 vol%), both in transient and stationary conditions. Fig. 4 reports the light-off curves for methane oxidation tests carried out under dry and wet stoichiometric conditions up to 1173 K; the temperatures corresponding to 10% and 50% CH_4 conversion, as well as the calculated reaction rates, are reported in Table 2. Under stoichiometric conditions, the milled sample shows better performance compared to the conventional IW catalyst, with the latter suffering from more significant activity loss due to the PdO-to-Pd decomposition both during the heating and the cooling ramp. The same trend was observed on 1 wt%Pd/CeO_2 samples (Fig. S6, ESI†), with the samples prepared by milling both outperforming the corresponding IW catalyst. In addition, the improved catalytic activity

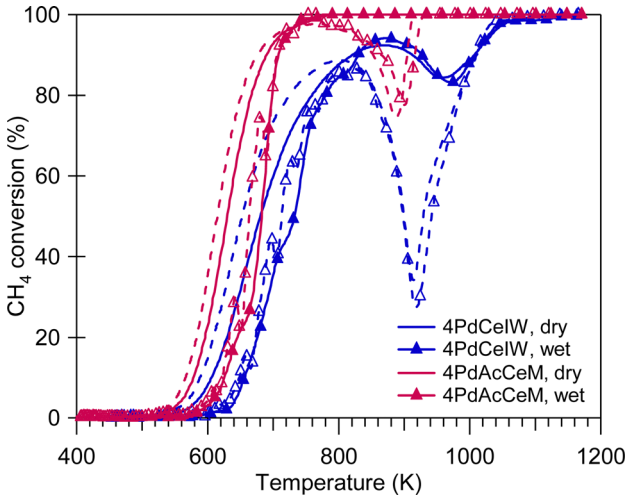

Fig. 4 Methane oxidation activity of 4PdAcCeM and 4PdCeIW under stoichiometric methane oxidation conditions, in a dry atmosphere and with 10 vol% H_2O added to the feed (wet). Solid line: heating; dashed line: cooling.

Table 2 Palladium loading, Pd atomic ratio, temperatures corresponding to 10% and 50% CH_4 conversion (T_{10} and T_{50}, respectively), and calculated reaction rates measured on 4PdCeIW and 4PdAcCeM samples in dry and wet conditions. For reaction rate calculations, conversion values are obtained from the 2nd light off heating ramp of methane oxidation experiments (Fig. 4, GHSV ≈ 400 000 h^{-1}) at temperatures ensuring $X_{CH4} < 5\%$, *i.e.* kinetic regime

Sample	Pd atomic[a] (%)	Measured Pd loading (wt%)	Feed	T_{10} (K)	T_{50} (K)	Rate ($\mu mol_{CH_4}\ g_{Pd}^{-1}\ s^{-1}$)
4PdCeIW	14.2	3.94	Dry	607	681	4.8[b]
			Wet (10%H_2O)	657	733	4.2[c]
4PdAcCeM	24.3	3.92	Dry	578	630	13.5[b]
			Wet (10%H_2O)	626	683	14.9[c]

[a] Measured at 673 K in AP-XPS chamber. [b] Measured at 563 K. [c] Measured at 613 K.

of 4PdAcCeM is maintained also in the presence of excess steam (10 vol%).

The quantitative results obtained by TPO experiments (Table S1, ESI†) exclude an effect of less palladium available for reaction on the 4PdCeIW sample, since previous results from our group showed that a lower amount of noble metal actively participating in the reaction would be linked to a minor amount of exchanged oxygen observed by TPO analysis.[42,55] Additionally, the difference in catalytic performance at high temperature can hardly be attributed to alternative reaction mechanisms occurring on the two samples. Partial oxidation and steam reforming of methane are reported as the main CH_4 conversion mechanisms for fuel rich mixtures at high temperatures.[18] However, in our previous work[44] these catalysts were observed to possess comparable steam reforming activity while here, under both dry and wet stoichiometric oxidation conditions, no CO formation is detected, suggesting that no partial oxidation is occurring; therefore, on the investigated Pd/CeO_2 samples full methane oxidation is still the driving conversion mechanism. Indeed, on all samples, irrespective of the gas feed conditions, the selectivity to CO_2 is equal to 100%. Consequently, having excluded the effect of a minor amount of palladium available for reaction and the occurrence of side reactions, the enhanced catalytic performance of the 4PdAcCeM milled sample can be primarily ascribed to the peculiar surface arrangement identified by NAP-XPS.

The improved steam deactivation resistance observed under transient wet oxidation conditions (Fig. 4) is maintained under prolonged exposure at lower temperature, as illustrated in Fig. 5 where the methane oxidation activity of 4PdCeIW and 4PdAcCeM held for 24 hours at 723 K in dry and wet conditions is reported. Below 773 K, the competitive adsorption of O_2 and H_2O on the catalyst surface and the accumulation of OH^- groups strongly hinder the oxygen transfer from the oxide support to the palladium species, and thus are indicated in the literature as the main steam inhibition mechanisms.[51,56] These effects can be mitigated by using redox active supports compared to Al_2O_3,[57,58] aiming at improving lattice oxygen transfer and maintaining the supported palladium species in an oxidized state. Here, the larger availability of ceria lattice oxygen species, observed by NAP-XPS under dry conditions on the milled sample, is able to efficiently inhibit the H_2O-induced deactivation, allowing the 4PdAcCeM catalyst to retain a higher conversion throughout the 24-hour isothermal period under a large excess of steam such as the one present in real NGV exhaust gases (above 10 vol%). Conversely, the higher tendency of the conventional 4PdCeIW catalyst to retain OH^- groups on the surface (Fig. 2C) results in a more pronounced loss of catalytic activity over the time-on-stream test (Fig. 5), which is further exacerbated by the addition of extra water vapor in the reaction feed.

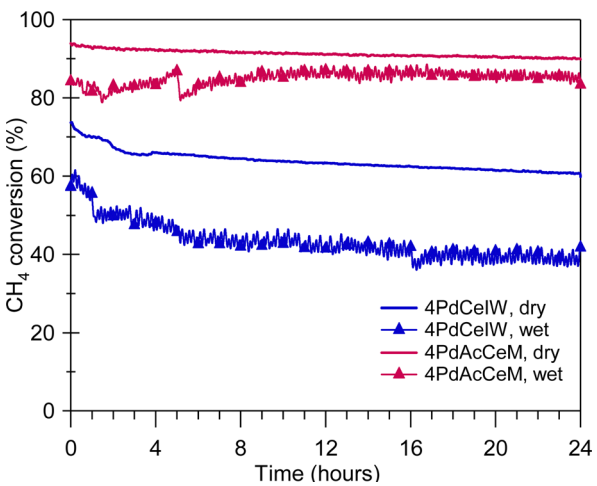

Fig. 5 Methane oxidation activity of 4PdAcCeM and 4PdCeIW under stoichiometric methane oxidation conditions held at 723 K for 24 hours; in a dry atmosphere (solid line) and with 10 vol% H_2O added to the feed (trace with symbols). Measured CO_2 selectivity on all samples: 100%.

In order to explain the observed differences in catalytic performance, XRD analysis appears to exclude a strong effect of the Pd particle size, which was instead linked to promoted reducibility to Pd^0 and reported as a key element in alumina-supported Pd catalysts.[33,59] However, the presence of surface amorphous phases, such as those observed on a similar milled sample under lean O_2 methane oxidation conditions,[42] would escape XRD detection, hindering a straightforward comparison between the two samples. Conversely, the combination of *in situ* XRD and NAP-XPS characterization (Fig. 1 and 2) presents additional insights into the surface environment of the investigated catalysts and suggests a predominant effect of the surface electronic state of palladium on CeO_2. On both samples, differently from what was observed under lean conditions, a combination of metallic and oxidized Pd species is observed, with the 4PdCeIW sample exhibiting predominant Pd^{2+} features both on the surface and in the bulk of the PdO particles, while a Pd^0/Pd^{2+} ratio closer to 0.5 is detected on the 4PdAcCeM sample (Fig. 3). In general, an undercoordinated PdO_x on Pd or PdO configuration was reported by both theoretical[39,53,60] and experimental works[42,54,61] as very active for the low temperature activation of methane under lean conditions, where the close interaction between neighboring Pd^0 and Pd–O species would lead to lower CH_4 activation energy.[52,53] In addition, a PdO-rich configuration was indicated as a key point for improved stability of $Pd/CeO_2/Al_2O_3$ catalysts under lean/rich oscillating NGV abatement conditions.[32,35]

Here, under stoichiometric conditions, we further reveal that on CeO_2 a less oxidized PdO_x state, with a Pd^0/Pd^{2+} ratio around 0.4–0.5, appears to be more favorable for CH_4 activation, as demonstrated by the performance of the 4PdAcCeM milled sample. This is in line with previous literature results, where a Pd core–PdO_x shell structure with a Pd^0/Pd^{2+} ratio close to 0.5 was reported as most favorable for CH_4 oxidation on Pd/CeO_2[54] and, similarly, as a strong promoter to reduce steam-induced deactivation on Pd/Al_2O_3.[32] However, both studies were carried out in the presence of excess O_2. Moreover, on the alumina support this structure had to be formed and maintained *via* repeated reducing pulses during reaction, while here we show that the CeO_2 support and the mechano-chemical synthesis method allow for the stabilization of such a structure throughout the reaction in a constant stoichiometric feed. NAP-XPS analysis with varying probing depths (Fig. 3) shows that no core–shell structure is formed in the Pd/CeO_2 system, thus likely contributing to the stability of the supported PdO_x particles. These results further suggest that the amount of PdO available for the reaction is important, but the source of O atoms plays a role as well: *i.e.*, mobile oxygen atoms supplied through ceria to undercoordinated PdO_x particles are likely more active than PdO nanoparticles well supported on Al_2O_3, suggesting that the Pd^0–PdO–CeO_x interface is responsible for enhanced methane oxidation activity under stoichiometric conditions. In addition, the NAP-XPS results in the O 1s range show that the peculiar configuration not only results in enhanced CH_4 activation performance but also in improved activity and stability in the presence of large quantities of H_2O, which are reported as strong competitors for surface O_2 adsorption sites[24,56] and thus lead to the formation of inactive palladium species.[62]

Conclusions

The catalytic abatement performance of Pd/CeO_2 catalysts prepared by solvent-free milling and incipient wetness impregnation methods was evaluated under stoichiometric reaction feed and followed *in situ* to reveal the Pd species involved in the CH_4 conversion under low O_2 pressure. Transient and stationary reaction tests show that the 4PdAcCeM milled sample displays higher methane oxidation activity and stability compared to 4PdCeIW, also in the presence of excess water in the feed. The *in situ* studies carried out during the reaction point at different Pd oxidation states involved under a 1 : 2 $CH_4:O_2$ gas feed, with a higher amount of metallic Pd species and significant mobility of the lattice Ce–O leading to higher activity and stability on the sample obtained by milling. Indeed, under a stoichiometric Air-to-Fuel (A/F) ratio, the optimal configuration for PdO_x particles supported on CeO_2 appears to be uniform palladium nanoparticles with a balanced ratio of Pd^0 and Pd^{2+} species (*ca.* 0.5), as exhibited by the milled sample. In addition, NAP-XPS results indicate that the enhanced lattice oxygen availability of the 4PdAcCeM catalyst, coupled with the optimal Pd^0/Pd^{2+} ratio around 0.5, are the main factors contributing to the improved activity and stability of the Pd/CeO_2 milled samples under O_2-deficient gas feed compositions. Conversely, on the reference sample prepared by the conventional IW technique, the PdO_x particles are maintained in a higher oxidation state, which proves to be less effective for CH_4 activation and more prone to steam-induced deactivation when no excess O_2 is available.

The differences observed between the Pd/CeO_2 system herein studied and the previous Pd/Al_2O_3 works reported in the literature, where nanosized Pd^0 particles displayed the highest activity and stability, highlight a much stronger role of CeO_2 as a support oxide. In addition, here we further show how the possibility to control the active Pd sites by a simple, one-pot mechanochemical process, leading to a Pd–Ce nanoscale arrangement that proves to be extremely active for CH_4 oxidation both in lean, stoichiometric and slightly rich atmospheres, can be highly interesting for industrial applications of the proposed synthesis process.

Author contributions

Maila Danielis: investigation, methodology, formal analysis, data curation, conceptualization, validation, writing – original draft. Núria J. Divins: investigation, methodology, data curation, formal analysis, writing – review & editing. Jordi Llorca: investigation, supervision, funding acquisition. Lluís Soler: investigation, formal analysis, data curation. Xènia Garcia: investigation, formal analysis. Isabel Serrano: investigation, formal analysis. Luis E. Betancourt: investigation, methodology, data

curation. Wenqian Xu: resources, data curation. José A. Rodríguez: supervision, resources, writing – review & editing. Sanjaya D. Senanayake: supervision, resources, funding acquisition. Sara Colussi: conceptualization, supervision, writing – review & editing. Alessandro Trovarelli: conceptualization, supervision, funding acquisition, writing – review & editing, project administration.

Conflicts of interest

There are no conflicts to declare.

Acknowledgements

M. D. and S. C. are grateful to Fondazione CRUI for Go for it Project CUP G29C20000830001. N. J. D. acknowledges the funding received from the European Union's Horizon 2020 research and innovation program under the Marie Sklodowska-Curie grant agreement No. 897197. L. S. is grateful to MICINN Ramon y Cajal program for an individual fellowship grant agreement RYC2019-026704-I. J. L. is a Serra Húnter Fellow and is grateful to the ICREA Academia program and projects MICINN/FEDER PID2021-124572OB-C31 and GC 2017 SGR 128. NAP-XPS experiments were performed at the CIRCE beamline at the ALBA Synchrotron with the collaboration of ALBA staff. The work carried out at Brookhaven National Laboratory was supported by the US Department of Energy, Chemical Sciences Division (DE-SC0012704). S. D. S. is supported by a US Department of Energy Early Career Award. The XRD experiments used resources of the Advanced Photon Source Beamline 17-BM (XRD) at Argonne National Laboratory, which is an Office of Science User Facility operated for the U.S. Department of Energy (DOE) Office of Science and was supported by the U.S. DOE under contract no. DE-AC02-06CH11357. This research used resources of the Advanced Light Source, a U.S. DOE Office of Science User Facility under contract no. DE-AC02-05CH11231.

References

1 T. Haasz, J. J. Gómez Vilchez, R. Kunze, P. Deane, D. Fraboulet, U. Fahl and E. Mulholland, *Energy Strategy Rev.*, 2018, **20**, 124–132.
2 Intergovernmental Panel on Climate Change, *Climate change 2014: mitigation of climate change: Working Group III contribution to the Fifth Assessment Report of the Intergovernmental Panel on Climate Change*, ed. O. Edenhofer, Cambridge University Press, New York, NY, 2014.
3 A. K. Datye and M. Votsmeier, *Nat. Mater.*, 2021, **20**, 1049–1059.
4 M. Gustafsson, N. Svensson, M. Eklund and B. Fredriksson Möller, *Transportation Research Part D: Transport and Environment*, 2021, **97**, 102911.
5 M. Clairotte, R. Suarez-Bertoa, A. A. Zardini, B. Giechaskiel, J. Pavlovic, V. Valverde, B. Ciuffo and C. Astorga, *Environ. Sci. Eur.*, 2020, **32**, 125.
6 H. Chen, J. He and X. Zhong, *J. Energy Inst.*, 2019, **92**, 1123–1136.
7 M. Hajbabaei, G. Karavalakis, K. C. Johnson, L. Lee and T. D. Durbin, *Energy*, 2013, **62**, 425–434.
8 A. M. Pourkhesalian, A. H. Shamekhi and F. Salimi, *Fuel*, 2010, **89**, 1056–1063.
9 H. Engerer and M. Horn, *Energy Policy*, 2010, **38**, 1017–1029.
10 C. Huang, W. Shan, Z. Lian, Y. Zhang and H. He, *Catal. Sci. Technol.*, 2020, **10**, 6407–6419.
11 A. Raj, *Johnson Matthey Technol. Rev.*, 2016, **60**, 228–235.
12 H. M. Cho and B.-Q. He, *Energy Convers. Manage.*, 2007, **48**, 608–618.
13 P. Einewall, P. Tunestål and B. Johansson, *Lean Burn Natural Gas Opearations vs. Stoichiometric Operation with EGR and a Three Way Catalyst*, SAE Special Publications, 2005, vol. 2005, pp. 343–362.
14 P. Lott and O. Deutschmann, *Emiss. Control Sci. Technol.*, 2021, **7**, 1–6.
15 D. Lou, Y. Ren, X. Li, Y. Zhang and X. Sun, *Energies*, 2020, **13**, 4905.
16 X. Liu, J. Chen, G. Zhang, Y. Wu, P. Shen, L. Zhong and Y. Chen, *J. Environ. Chem. Eng.*, 2021, **9**, 105570.
17 D. Jiang, K. Khivantsev and Y. Wang, *ACS Catal.*, 2020, **10**, 14304–14314.
18 H. Stotz, L. Maier and O. Deutschmann, *Top. Catal.*, 2017, **60**, 83–109.
19 M. Monai, T. Montini, R. J. Gorte and P. Fornasiero, *Eur. J. Inorg. Chem.*, 2018, 2884–2893.
20 R. J. Farrauto, *Science*, 2012, **337**, 659–660.
21 M. Cargnello, J. J. D. Jaen, J. C. H. Garrido, K. Bakhmutsky, T. Montini, J. J. C. Gamez, R. J. Gorte and P. Fornasiero, *Science*, 2012, **337**, 713–717.
22 R. Sajiv Kumar, R. E. Hayes and N. Semagina, *Catal. Today*, 2021, **382**, 82–95.
23 P. Granger, *Catal. Sci. Technol.*, 2017, **7**, 5195–5211.
24 O. Mihai, G. Smedler, U. Nylén, M. Olofsson and L. Olsson, *Catal. Sci. Technol.*, 2017, **7**, 3084–3096.
25 N. J. Divins, A. Braga, X. Vendrell, I. Serrano, X. Garcia, L. Soler, I. Lucentini, M. Danielis, A. Mussio, S. Colussi, I. J. Villar-Garcia, C. Escudero, A. Trovarelli and J. Llorca, *Nat. Commun.*, 2022, **13**, 5080.
26 A. Mussio, M. Danielis, N. J. Divins, J. Llorca, S. Colussi and A. Trovarelli, *ACS Appl. Mater. Interfaces*, 2021, **13**, 31614–31623.
27 P. H. Ho, J.-W. Woo, R. Feizie Ilmasani, J. Han and L. Olsson, *Ind. Eng. Chem. Res.*, 2021, **60**, 6596–6612.
28 K. A. Karinshak, P. Lott, M. P. Harold and O. Deutschmann, *ChemCatChem*, 2020, **12**, 3712–3720.
29 A. E. Hughes, N. Haque, S. A. Northey and S. Giddey, *Resources*, 2021, **10**, 93.
30 H. Xiong, D. Kunwar, D. Jiang, C. E. García-Vargas, H. Li, C. Du, G. Canning, X. I. Pereira-Hernandez, Q. Wan, S. Lin, S. C. Purdy, J. T. Miller, K. Leung, S. S. Chou, H. H. Brongersma, R. ter Veen, J. Huang, H. Guo, Y. Wang and A. K. Datye, *Nat. Catal.*, 2021, **4**, 830–839.

31 S. Colussi, P. Fornasiero and A. Trovarelli, *Chin. J. Catal.*, 2020, **41**, 938–950.
32 T. Franken, M. Roger, A. W. Petrov, A. H. Clark, M. Agote-Arán, F. Krumeich, O. Kröcher and D. Ferri, *ACS Catal.*, 2021, **11**, 4870–4879.
33 J. Chen, J. Zhong, Y. Wu, W. Hu, P. Qu, X. Xiao, G. Zhang, X. Liu, Y. Jiao, L. Zhong and Y. Chen, *ACS Catal.*, 2020, **10**, 10339–10349.
34 J. Chen, Y. Wu, W. Hu, P. Qu, G. Zhang, P. Granger, L. Zhong and Y. Chen, *Appl. Catal., B*, 2020, **264**, 118475.
35 J. Nilsson, P.-A. Carlsson, N. M. Martin, E. C. Adams, G. Agostini, H. Grönbeck and M. Skoglundh, *J. Catal.*, 2017, **356**, 237–245.
36 D. Ferri, M. Elsener and O. Kröcher, *Appl. Catal., B*, 2018, **220**, 67–77.
37 F. Huang, J. Chen, W. Hu, G. Li, Y. Wu, S. Yuan, L. Zhong and Y. Chen, *Appl. Catal., B*, 2017, **219**, 73–81.
38 S. K. Matam, G. L. Chiarello, Y. Lu, A. Weidenkaff and D. Ferri, *Top. Catal.*, 2013, **56**, 239–242.
39 A. Hellman, A. Resta, N. M. Martin, J. Gustafson, A. Trinchero, P.-A. Carlsson, O. Balmes, R. Felici, R. van Rijn, J. W. M. Frenken, J. N. Andersen, E. Lundgren and H. Grönbeck, *J. Phys. Chem. Lett.*, 2012, **3**, 678–682.
40 I. Friberg, A. H. Clark, P. H. Ho, N. Sadokhina, G. J. Smales, J. Woo, X. Auvray, D. Ferri, M. Nachtegaal, O. Kröcher and L. Olsson, *Catal. Today*, 2021, **382**, 3–12.
41 K. G. Rappé, C. DiMaggio, J. A. Pihl, J. R. Theis, S. H. Oh, G. B. Fisher, J. Parks, V. G. Easterling, M. Yang, M. L. Stewart and K. C. Howden, *Emiss. Control Sci. Technol.*, 2019, **5**, 183–214.
42 M. Danielis, L. E. Betancourt, I. Orozco, N. J. Divins, J. Llorca, J. A. Rodríguez, S. D. Senanayake, S. Colussi and A. Trovarelli, *Appl. Catal., B*, 2021, **282**, 119567.
43 M. Danielis, S. Colussi, C. de Leitenburg, L. Soler, J. Llorca and A. Trovarelli, *Angew. Chem., Int. Ed.*, 2018, **57**, 10212–10216.
44 M. Danielis, S. Colussi, J. Llorca, R. H. Dolan, G. Cavataio and A. Trovarelli, *Ind. Eng. Chem. Res.*, 2021, **60**, 6435–6445.
45 P. J. Chupas, K. W. Chapman, C. Kurtz, J. C. Hanson, P. L. Lee and C. P. Grey, *J. Appl. Crystallogr.*, 2008, **41**, 822–824.
46 B. H. Toby and R. B. Von Dreele, *J. Appl. Crystallogr.*, 2013, **46**, 544–549.
47 D. R. Mullins, S. H. Overbury and D. R. Huntley, *Surf. Sci.*, 1998, **409**, 307–319.
48 M. M. Natile and A. Glisenti, *Surf. Sci. Spectra*, 2021, **13**, 17.
49 R. Pugliese and G. Paolucci, Atomic calculation of photo-ionization cross-sections and asymmetry parameters, (accessed September 7, 2022), **https://vuo.elettra.eu/services/elements/WebElements.html**.
50 S. Colussi, A. Trovarelli, E. Vesselli, A. Baraldi, G. Comelli, G. Groppi and J. Llorca, *Appl. Catal., A*, 2010, **390**, 1–10.
51 X. Li, X. Wang, K. Roy, J. A. van Bokhoven and L. Artiglia, *ACS Catal.*, 2020, **10**, 5783–5792.
52 R. J. Bunting, X. Cheng, J. Thompson and P. Hu, *ACS Catal.*, 2019, **9**, 10317–10323.
53 N. M. Kinnunen, J. T. Hirvi, M. Suvanto and T. A. Pakkanen, *J. Phys. Chem. C*, 2011, **115**, 19197–19202.
54 K. Murata, D. Kosuge, J. Ohyama, Y. Mahara, Y. Yamamoto, S. Arai and A. Satsuma, *ACS Catal.*, 2020, **10**, 1381–1387.
55 M. Danielis, S. Colussi, C. de Leitenburg, L. Soler, J. Llorca and A. Trovarelli, *Catal. Sci. Technol.*, 2019, **9**, 4232–4238.
56 R. Gholami, M. Alyani and K. Smith, *Catalysts*, 2015, **5**, 561–594.
57 W. Barrett, J. Shen, Y. Hu, R. E. Hayes, R. W. J. Scott and N. Semagina, *ChemCatChem*, 2020, **12**, 944–952.
58 M. Monai, T. Montini, C. Chen, E. Fonda, R. J. Gorte and P. Fornasiero, *ChemCatChem*, 2015, **7**, 2038–2046.
59 J. J. Willis, A. Gallo, D. Sokaras, H. Aljama, S. H. Nowak, E. D. Goodman, L. Wu, C. J. Tassone, T. F. Jaramillo, F. Abild-Pedersen and M. Cargnello, *ACS Catal.*, 2017, **7**, 7810–7821.
60 N. M. Martin, M. Van den Bossche, A. Hellman, H. Grönbeck, C. Hakanoglu, J. Gustafson, S. Blomberg, N. Johansson, Z. Liu, S. Axnanda, J. F. Weaver and E. Lundgren, *ACS Catal.*, 2014, **4**, 3330–3334.
61 Y. Mahara, K. Murata, K. Ueda, J. Ohyama, K. Kato and A. Satsuma, *ChemCatChem*, 2018, **10**, 3384–3387.
62 P. Velin, F. Hemmingsson, A. Schaefer, M. Skoglundh, K. A. Lomachenko, A. Raj, D. Thompsett, G. Smedler and P. Carlsson, *ChemCatChem*, 2021, **13**, 3765–3771.